Inhibition of vibrational energy flow within an aromatic scaffold via heavy atom effect

Majid Hassani,[1] (iD) Christopher J. Mallon,[1] Judith N. Monzy,[2] (iD) Andrew J. Schmitz,[1] Scott H. Brewer,[2] (iD) Edward E. Fenlon,[2,a)] (iD) and Matthew J. Tucker[1,a)] (iD)

AFFILIATIONS

[1] Department of Chemistry, University of Nevada, Reno, Nevada 89557, USA

[2] Department of Chemistry, Franklin & Marshall College, Lancaster, Pennsylvania 17604-3003, USA

a)Authors to whom correspondence should be addressed: edward.fenlon@fandm.edu and mtucker@unr.edu

ABSTRACT

The regulation of intramolecular vibrational energy redistribution (IVR) to influence energy flow within molecular scaffolds provides a way to steer fundamental processes of chemistry, such as chemical reactivity in proteins and design of molecular diodes. Using two-dimensional infrared (2D IR) spectroscopy, changes in the intensity of vibrational cross-peaks are often used to evaluate different energy transfer pathways present in small molecules. Previous 2D IR studies of *para*-azidobenzonitrile (PAB) demonstrated that several possible energy pathways from the N_3 to the cyano-vibrational reporters were modulated by Fermi resonance, followed by energy relaxation into the solvent [Schmitz *et al.*, J. Phys. Chem. A **123**, 10571 (2019)]. In this work, the mechanisms of IVR were hindered via the introduction of a heavy atom, selenium, into the molecular scaffold. This effectively eliminated the energy transfer pathway and resulted in the dissipation of the energy into the bath and direct dipole–dipole coupling between the two vibrational reporters. Several structural variations of the aforementioned molecular scaffold were employed to assess how each interrupted the energy transfer pathways, and the evolution of 2D IR cross-peaks was measured to assess the changes in the energy flow. By eliminating the energy transfer pathways through isolation of specific vibrational transitions, through-space vibrational coupling between an azido (N_3) and a selenocyanato (SeCN) probe is facilitated and observed for the first time. Thus, the rectification of this molecular circuitry is accomplished through the inhibition of energy flow using heavy atoms to suppress the anharmonic coupling and, instead, favor a vibrational coupling pathway.

Published under an exclusive license by AIP Publishing. https://doi.org/10.1063/5.0153760

INTRODUCTION

After more than 25 years, two-dimensional infrared (2D IR) spectroscopy has become the premiere ultrafast technique to characterize vibrational dynamics, including drug binding events, protein folding events via transient 2D IR, energy transfer in materials, population exchange, and properties of ion channels in cell membranes.[2–12] 2D IR uniquely separates the homogeneous and inhomogeneous contributions to absorption lineshapes, revealing the phenomenon of spectral diffusion. The temporal dynamics of spectral diffusion can be measured through the center line slope of the contours in the 2D IR spectra. The behavior of the center line slope (CLS) matches that of the frequency–frequency correlation functions (FFCFs), which reveal the localized solvent dynamics in the heterogeneous solutions, which play an important role in reactivity.[13–16] Another attractive feature of 2D IR spectroscopy comes from its ability to determine the types of interactions between multiple vibrational transitions within a molecular scaffold via the appearance and behavior of cross-peaks. For example, vibrational coupling, i.e., mechanical and/or dipole–dipole coupling,[4,17,18] results in cross-peaks in the 2D IR spectrum at the earliest waiting times and then decays over time.[2,4,19–21] On the other hand, cross-peaks that become more intense as a function of waiting time are indicative of population exchange or vibrational energy relaxation (VER).[1,22] If the VER entails several vibrational modes becoming delocalized within a molecular system to overlap in their vibrational motion, it is referred to as intramolecular vibrational energy redistribution (IVR). The propagation of thermal energy is delayed because the energy absorbed by one vibration must flow through the molecular scaffold until it finally reaches another vibration.[23–26] Theoretical[27–32] and experimental studies of VER have discussed different factors influencing the rates of thermal energy flow, relative directions of heat flow, and characteristics of diffusive/ballistic transport.[23,33–39] Oftentimes, multiple dark states are involved in the

energy transfer pathways, which creates challenges in predicting the energy flow within the molecule and determining the rate.[24] However, several methods have been developed to successfully design molecules that decouple certain modes to guide the preferred route of energy flow.[1,22,24,40]

The ability to guide VER within a molecular system would enhance many chemical processes, including synthetic chemistry[24,39–42] and the development of molecular electronics.[33,34,43–45] It can also influence the three dimensional structures of molecular systems.[6,26,46,47] Furthermore, protein functionality is significantly influenced by VER affecting hydrogen bonding,[48] secondary and tertiary structure formation,[32] and allosteric communication.[49,50] Thus, guiding VER within a molecule provides a way to influence these processes in a desirable way or even inhibit them if necessary.

Recently, 2D IR studies have investigated the necessary elements for guiding energy flow within molecular scaffolds and factors that influence the overall pathway. Some studies involving transition metals have suggested that heavy atoms can influence transfer efficiency, the direction of relaxation, and the contribution of solvents to IVR.[35,51,52] 2D IR studies by Zheng and co-workers have reported the influence on the rates of intermolecular energy transfer over different distances and orientations between vibrations of a wide array of molecular systems.[24,39,40,43,44,46] Rubtsov and co-workers have developed relaxation-assisted two-dimensional infrared spectroscopy (RA 2DIR)[23] to evaluate the energy transfer rates between various vibrational mode pairs over a variety of distances.[26,53–55] The energy transfer rates were found to be highly dependent on bond length[44,47,54] and temperature.[55]

Recently, Tucker and co-workers uncovered a method to predict the most probable energy transfer pathway through coupled dark modes via the assessment of third order coupling parameters.[1] In these studies, *para*-azidobenzonitrile (PAB) and *para*-methylazidobenzonitrile (PAMB) were shown to exhibit several possible energy pathways from the N_3 to the cyano-vibrational reporters facilitated by Fermi resonant modes (Fig. 1).

In this study, several structural variations of the molecular scaffold are employed to interrupt these energy transfer pathways, and the evolution of 2D IR cross-peaks was measured to assess the changes in the energy flow. By isolating specific vibrational transitions and, thus, hindering the energy transfer pathway, dipole–dipole coupling was facilitated, allowing direct coupling to be detected between N_3 and weak selenocyanato (SeCN) vibrational modes for the first time. A comparison between experimentally determined vibrational coupling and the theoretical analysis of coupling strengths for the studied molecular systems was made. Differences in the energy of the vibrational transitions, transition dipole
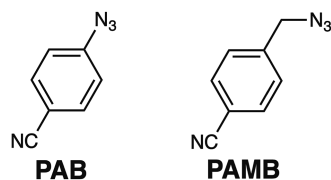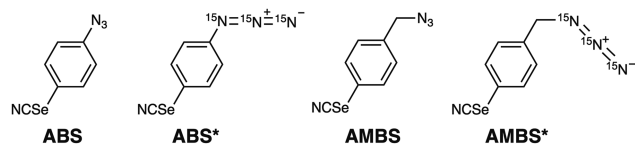

FIG. 2. Structures of 4-azidobenzoselenocyanate (ABS), triple-15N-labeled 4-azidobenzoselenocyanate (ABS*), 4-azidomethylbenzoselenocyanate (AMBS), and triple-15N-labeled 4-azidomethylbenzoselenocyanate (AMBS*).

strengths, and angle between the dipoles are addressed in terms of the observed couplings. Thus, the ability of heavy atoms to suppress energy transfer pathways and thereby influence the flow of energy in molecular circuitry is effectively demonstrated.

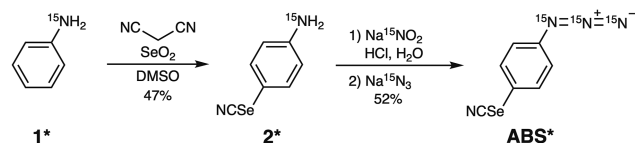## MATERIALS AND METHODS

Sample preparation

The vibrational coupling between N_3 and SeCN vibrational reporters was studied using 4-azidobenzoselenocyanate (ABS), triple-15N-labeled 4-azidobenzoselenocyanate (ABS*), 4-azidomethylbenzoselenocyanate (AMBS), and triple-15N-labeled 4-azidomethylbenzoselenocyanate (AMBS*); see Fig. 2. The complete synthetic details are given in the supplementary material.

The same synthetic route was used to prepare ABS and ABS*, as illustrated for ABS* in Scheme 1. The electrophilic aromatic substitution of 15N-labeled aniline (1*) by triselenium dicyanide, generated *in situ* from selenium dioxide and malononitrile, produced labeled selenocyanate 2* in modest yield.[56] The triple-labeled N_3 isotopologue of ABS was obtained by diazonium ion formation with 15N-labeled sodium nitrite followed by the addition of triple-labeled sodium azide. This two-step sequence gave a 52% yield of ABS*. The unlabeled synthesis gave an 87% yield of selenocyanate **2** and a 34% yield of **ABS**.

The synthesis of AMBS was accomplished by the four-step, two-pot sequence outlined in Scheme 2. Aniline **3** was diazotized with acidic sodium nitrite followed by the addition of potassium selenocyanate to provide intermediate **4** in modest yield. The conversion of the alcohol of **4** to the mesylate leaving group, followed by an S_N2 reaction with the azide anion, provided AMBS in 15% yield after purification. The same method was used to synthesize **AMBS***, but triple-15N-labeled sodium azide was used to provide the product in 28% yield.

Linear and 2D IR methods

Solutions of 30–40 mM ABS, AMBS, ABS*, and AMBS* in tetrahydrofuran (THF) were prepared for both 2D IR and FTIR

FIG. 1. Structure of *para*-azidobenzonitrile (PAB) and *para*-methylazidobenzonitrile (PAMB).

SCHEME 1. Two-pot preparation of ABS* by selenocyanation, diazonium ion formation, and azide treatment.
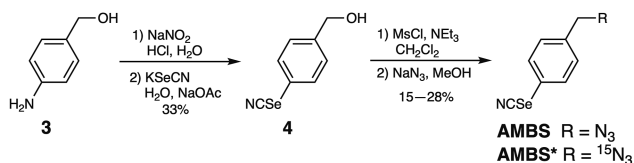
SCHEME 2. Two-pot preparation of AMBS by selenocyanation, mesylate formation, and azide displacement.

experiments. The FTIR and 2D IR samples were placed in a Harrick sample cell with CaF$_2$ windows and a pathlength of 56 μm for ABS and AMBS and a 100 μm pathlength for ABS* and AMBS*. The linear infrared spectra were measured using a Nicolet 6700 FTIR. To determine the full width at half maximum (FWHM), each transition was fit to a Gaussian profile, $y = A \cdot e^{-4 \ln(2)(x-x_c)^2/w^2}$.

2D IR experiments were performed in the boxCARs geometry[57–59] with Fourier-transform 80-fs pulses with a central wavelength ranging from 4650 to 4750 nm depending on the sample. Three laser pulses, each with an energy of ~1 μJ, with wave vectors k_1, k_2, and k_3, were incident on the samples to generate a signal in the direction $k_{sig} = -k_1 + k_2 + k_3$ with time-ordering of 123 (rephasing) and 213 (nonrephasing). To acquire absorptive spectra, the rephasing and nonrephasing 2D frequency spectra were properly phased and combined.[58] The waiting time, T, between the second and third pulses was varied from 0 to 6 ps in order to measure the dynamics observed in the 2D line shapes. After appropriate Fourier transforms along the coherence, τ, and detection, t, axes, the 2D IR spectra are plotted ω_τ vs ω_t. The vibrational relaxation times, T_{10}, were estimated from the decay of the on-diagonal signal strengths of the v = 0 → v = 1 transition in the 2D IR spectrum at different waiting times and fitted to an exponential decay, $A = A_0 e^{-T/T_{10}}$.

Coupling values are obtained from the experimental 2D IR data using the equation $\beta_{1,2}^{(ex)} = \frac{|E_2 - E_1|}{2\sqrt{1+\frac{\Delta}{\Delta_{12}}}}$. Here, E_1 and E_2 are the observed energies of the coupled transitions, Δ_{12} is the observed off-diagonal anharmonicity between the peak positions of the positive and negative contours of the cross-peaks, and Δ is the geometric average of the anharmonicities of the fundamental transitions, defined by the difference between the peak positions of the positive and negative contours of the diagonal peaks. This equation comes from the perturbative treatment of the anharmonicity in a system of two coupled harmonic oscillators of the first order.[2]

Computational methods

Both Gaussian09 and Gaussian16[60] were used to perform density functional theory (DFT) calculations of ABS, AMBS, ABS*, and AMBS* at the B3LYP/6-31+G (d,p) level of theory. An implicit solvation model of THF was used through all calculations with the self-consistent reaction field (SCRF) in the conducting polarizable continuum model (CPCM). The optimizations were followed by harmonic frequency calculations to obtain frequency and energy data. Anharmonic frequency calculations were performed to identify the possible Fermi resonances that appear in the infrared spectra.

The normal mode coordinates obtained from the frequency calculations were used to determine the coupling constant between the N$_3$ and SeCN reporters using the finite difference method (FDM).[61] The coupling values in this approach were obtained after perturbing the optimized structure by a small amount (0.03 times the oscillation amplitude in Å) along the N$_3$ and SeCN normal modes. Single point energy calculations were performed after perturbation and used to calculate the vibrational coupling through the second derivative of the energy with respect to both normal modes. The second-order central difference scheme was utilized to calculate the mixed second derivative of the potential energy surface.

The dihedral angle along the C–N bond connecting the phenyl group with the N$_3$ reporter in ABS was rotated from 90° to 450° to map out the potential energy surface along this degree of freedom. Likewise, the C–N bond connecting the methyl group with the N$_3$ reporter in AMBS was rotated from 0° to 360°. The resulting structures at each step of the rotation were allowed to relax to a minimum energy with the dihedral angle fixed. The relative energies were then plotted as a function of dihedral angle. A sampling of structures near the local minima, defined to be approximately within the thermal distribution at room temperature (~0.59 kcal/mol), was then used to calculate the average angles and distances between the SeCN and N$_3$ dipoles, as well as their dipole moment strengths and coupling constants obtained in FDM calculations.

RESULTS AND DISCUSSION

Linear IR spectra of ABS and AMBS

FTIR measurements were conducted on ABS and AMBS in THF. The linear IR spectrum of ABS in THF exhibits three transitions observed at 2092, 2128, and 2154 cm^{-1}, as shown in Fig. 3(a). For the spectrum of ABS, the asymmetric stretch of the N$_3$ transition appears at 2092 cm^{-1}, and the SeCN stretch is located at 2154 cm^{-1}. The third transition centered at 2128 cm^{-1} arises from a Fermi resonance, an "accidental" resonance of a combination band consisting of two ring modes with the fundamental N$_3$ transition, which has been reported in the previous work on similar molecular scaffolds.[1,62–65] The linear IR spectrum of AMBS in THF also had three distinct transitions located at 2098, 2130, and 2154 cm^{-1} corresponding to the N$_3$, Fermi, and SeCN transitions, respectively. As a result of adding one methylene group between the benzene ring and the azide, a 6 cm^{-1} blue-shift was observed in the vibrational frequency of the N$_3$ transition and a negligible shift in the Fermi transitions. A shift in frequency of the N$_3$ transition closer to the Fermi transition likely indicates a slight decoupling of the ring modes from the N$_3$ transition. The coupled vibrational frequencies are expected to be more separated from the original uncoupled frequencies holding to a simple bilinear coupling model. Thus, some decoupling has occurred. On the other hand, the SeCN stretching frequency remains independent of the molecular structure due to the heavy atom effect.[66,67]

The spectral profile of AMBS shows a weak transition observed around 2130 cm^{-1}, which was detected in the linear IR spectrum. The identity of this transition is further confirmed by cross-peaks detected in the 2D IR spectrum (discussed below) due to the anharmonic (Fermi) coupling. However, the intensity of this Fermi resonance is much weaker than ABS because of the separation of the benzene ring from the N$_3$ group using one carbon atom.[68] This reduction of the anharmonic coupling was observed in our earlier work on PAB and PAMB.[1] In the same work, it was found that this loss of anharmonic coupling between the N$_3$ group and the lower
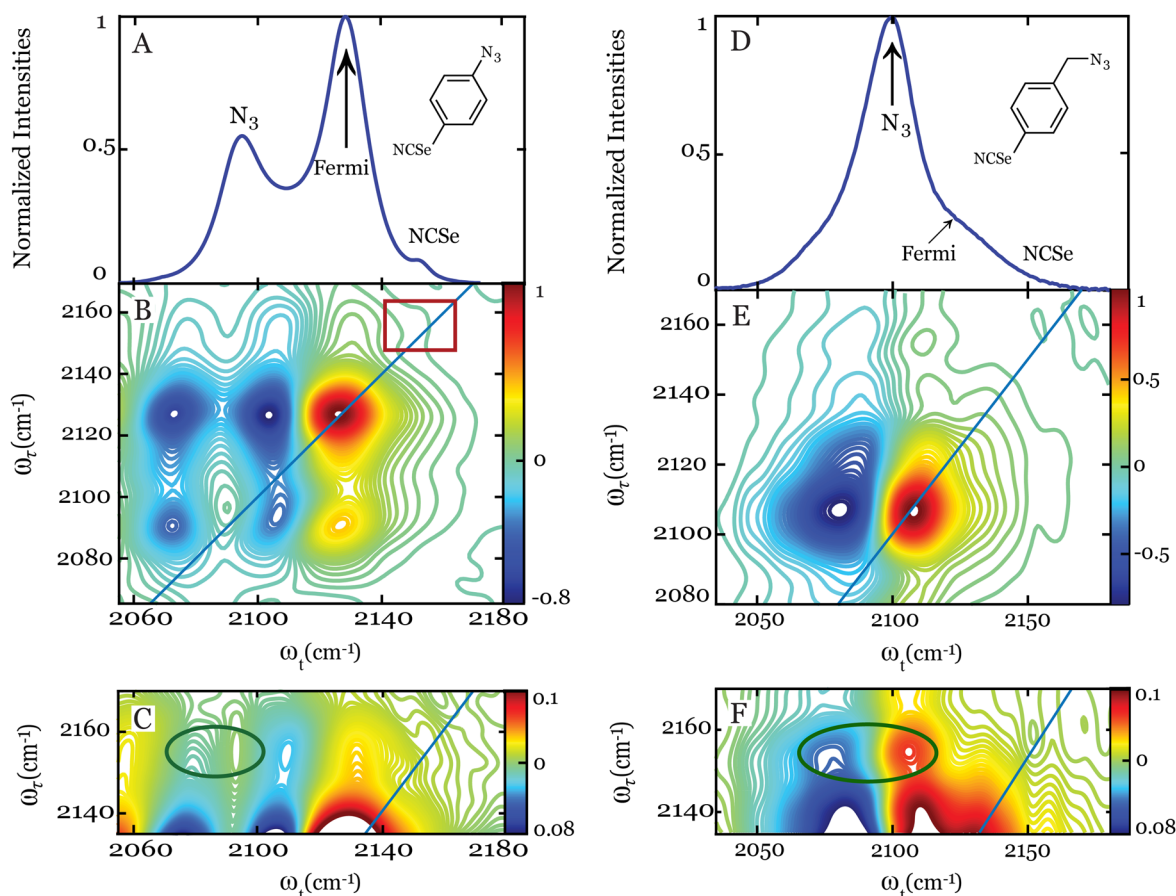
FIG. 3. FTIR spectra of (a) ABS and (d) AMBS in THF and absorptive 2D IR spectra of (b) ABS and (e) AMBS in THF at T = 800 fs. Panels (c) and (f) show the expanded cross-peak region of panels (b) and (e), respectively.

energy ring modes through the Fermi resonance leads to a much slower energy transfer within the vibrational scaffold and slightly alters the transfer pathway.[1]

The calculated FWHM for ABS, as obtained from fitting to Gaussian line shapes, was 19.3, 18.6, and 9.1 cm^{-1} for N$_3$, Fermi, and SeCN transitions, respectively. The linewidths of the two fundamental transitions obtained for AMBS were similar to that of ABS, exhibiting FWHMs of 23.9 and 9.1 cm^{-1} for the N$_3$ and SeCN transitions, respectively. However, the FWHM of the Fermi transition broadened to 29.31 cm^{-1} in AMBS is likely due to a broader distribution of modes coupling to the fundamental transition.[68] The broader distribution of coupled dark ring modes will have less intensity as a result of the decreased mixing within the bilinear coupling matrix. The experimental IR intensity ratio between the fundamental N$_3$ transition and Fermi resonance was 1:1.79 for ABS compared to 1:0.22 for AMBS. It is clear that the addition of methylene between the benzene ring and azide reporter causes the strength of Fermi resonance to decrease as the azide reporter is brought into resonance with different combination bands of the benzene ring. Furthermore, these differences in the spectral profile can easily be replicated by varying the strength of the anharmonic coupling in the coupling matrix by a few wavenumbers.

Computations

Ab initio density functional theory (DFT) calculations of anharmonic frequencies were performed after geometry optimization in order to confirm the identity of the N$_3$ and SeCN modes and determine the possible anharmonic modes that contribute to the Fermi resonance. The results of the DFT calculations confirmed the identities of the two transitions in the spectral region corresponding to the N$_3$ asymmetric stretch and the SeCN stretch based on the values of their relative vibrational frequencies. A correction factor of 0.9675 was applied to match the experimental and calculated SeCN vibrational frequencies at 2154 cm^{-1}. A summary of the calculated and experimental vibrational frequencies of both vibrational reporters and the suspected Fermi resonances (combination bands of low frequency ring modes) is given in Table I. The SeCN vibration in ABS, AMBS, ABS*, and AMBS* was all predicted to be at the same frequency, which agrees with the experimental results. The calculated N$_3$ asymmetric stretch frequencies were 2119, 2101, 2055, and 2038 cm^{-1} for ABS, AMBS, ABS*, and AMBS*, respectively. It should be noted that the modes involving the Fermi resonances were not determined solely based on resonance with the fundamental N$_3$ frequency. Instead, the Fermi resonances were determined

TABLE I. Experimental and calculated transition frequencies for the N_3, SeCN, and Fermi resonances.

Sample	Experimental (cm^{-1})			Calculated (cm^{-1})		
	ω_{N_3}	ω_{Fermi}	ω_{SeCN}	ω_{N_3}	ω_{Fermi}	ω_{SeCN}
ABS	2092	2128	2154	2119	2125	2154
AMBS	2098	2130	2154	2101	2113	2154
ABS*	2037	2070	2154	2055	2084	2154
AMBS*	2031	2055	2154	2038	2084	2154

from anharmonic calculations by the combination band with the highest predicted intensity that was close to the region in which the Fermi resonance was observed experimentally.

2D IR spectroscopy

2D IR spectra of ABS and AMBS at early waiting times are shown in Figs. 3(b) and 3(e), respectively. Akin to the linear IR spectrum, the N_3 $\nu = 0 \rightarrow \nu = 1$ transitions appear along the diagonal at $\omega_t = \omega_\tau = 2092$ cm^{-1} and $\omega_t = \omega_\tau = 2107$ cm^{-1} for ABS and AMBS, respectively. The negative contours red-shifted along the ω_t axis represent $\nu = 1 \rightarrow \nu = 2$ transitions resulting from the anharmonic nature of the oscillations. The diagonal anharmonicities of the N_3 transitions for ABS and AMBS are ~26.4 ± 0.4 and 20 ± 6 cm^{-1}, respectively. The vibrational lifetime for the N_3 transition was measured to be ~0.28 ± 0.04 ps (Fig. S4). The rapid population decay is a result of the fast energy transfer to the ring modes, as mentioned above.

Another diagonal transition corresponding to the Fermi resonance seen in the linear IR spectra for ABS is located at $\omega_t = \omega_\tau = 2130$ cm^{-1}. A strong cross-peak, $\omega_t = 2134$ cm^{-1} and $\omega_\tau = 2091$ cm^{-1}, decreases in intensity as a function of waiting time in the 2D IR spectrum of ABS. This is attributed to strong anharmonic coupling, ~12.4 cm^{-1}, between the N_3 and Fermi transitions, as calculated using the coupling equation above. Although the ^{13}C nuclear magnetic resonance (NMR) spectrum indicates the presence of SeCN, it should be noted that the expected transition is not observed in the 2D IR spectrum of ABS at $\omega_t = \omega_\tau = 2154$ cm^{-1} due to its extremely weak transition dipole strength, ~0.06 D.[69] However, the presence of this weak transition is revealed by the off-diagonal cross-peaks representing coupling between the N_3 and the SeCN transitions, located at $\omega_t = 2154$ cm^{-1} and $\omega_\tau = 2091$ cm^{-1} [shown by green ovals in Fig. 3(c)]. Upon careful examination of the spectrum, a small elongation of the positive-going transition toward higher energy is found along ω_t, highlighted by the red rectangle in Fig. 3(b). This rectangle indicates the suspected location of the SeCN transition. To verify its location, the vibrational transition of the SeCN oscillator is clearly shown for another isotopically labeled scaffold, documented in the supplementary material (Fig. S6).

The mechanism of coupling is very different from the prior scaffold, PAB, investigated for its thermal energy flow, i.e., energy transfer.[1] In the PAB scaffold, the thermal energy flow occurred from the N_3 transition to several anharmonically coupled modes, eventually reaching the nitrile group.[1] The current scaffold, ABS,

shows that this energy pathway has been interrupted by the presence of the Se atom, taking advantage of the well-known heavy atom effect, which isolates the vibration preventing rapid damping and energy leakage to the rest of the molecule.[66,67] This change in the mechanism of vibrational dynamics is indicated by the lack of growth observed for the off-diagonal cross-peak between the SeCN and N_3 transitions (see Figs. S1 and S2 in the supplementary material).

Instead, the 2D IR spectrum of ABS demonstrates for the first time the presence of dipole–dipole coupling between weak (almost undetected) SeCN and the strong N_3 transitions. This observation further suggests that the intensity mixing that occurs in the coupling matrix provides a way to observe modes with significantly weak transition dipole strengths, such as SeCN. These extremely weak modes need only be coupled to another mode with a much stronger dipole strength, such as N_3. A dipole–dipole coupling strength of ~21 cm^{-1} was determined between the N_3 and SeCN modes from cross-peaks for the estimated distance of ~6.13 Å from the computed structure. This ability to hinder the thermal pathway provides an avenue to change the flow of energy within a molecule, which has utility in developing molecular circuitry. In addition, this methodology allows the measurement of distances with these vibrational reporters in other larger scaffolds where energy transfer can bev problematic.

To further evaluate the ability to suppress energy transfer pathways, the AMBS scaffold was compared to PAMB, which contained at least two thermal energy pathways from the N_3 to the CN transitions.[1] Similar to PAMB, the AMBS 2D IR spectrum displays a significant decrease in the Fermi resonance bands, $\omega_t = \omega_\tau = 2130$ cm^{-1}, and their off-diagonal cross-peaks, $\omega_t = 2107$ cm^{-1} and $\omega_\tau = 2130$ cm^{-1}, indicating that the first part of the energy transfer pathway is intact but with a reduced rate.[1] The experimental 2D IR results also show that the coupling between the azido and Fermi transitions reduces by ~1–2 cm^{-1} in AMBS as compared with ABS. The rate of energy transfer is affected by both this reduction and the addition of the carbon atom between the benzene ring and the N_3 group.[1] The vibrational lifetime measured for the N_3 transition was ~0.89 ± 0.06 ps (Fig. S4). This population decay is 3.2 times longer than the ABS scaffold due to the reduction of anharmonic coupling and less damping of the energy.

As observed in ABS, all the off-diagonal cross-peaks in the spectrum decay as a function of waiting time from the earliest times (see the supplementary material, Figs. S1 and S2), indicating the loss of energy transfer to the SeCN transition. Once again, the Se atom was able to interrupt the multiple thermal transfer pathways between the N_3 and CN transitions in the prior PAB scaffold. Despite the slight decrease in coupling strength between the N_3 and Fermi transitions mentioned above, the thermal pathway between the N_3 and Fermi transitions is still open, as indicated by the delocalization of vibration shown in the energy density calculation (computed and shown below). Analysis of the cross-peaks seen between the SeCN and N_3 transitions in AMBS revealed a similar coupling strength of ~19.6 cm^{-1} to that observed for ABS over the estimated distance of 6.9 Å from the computed structure. It should be noted that even though the structural distance is slightly larger, the dipole moment orientation is expected to be more favorable, leading to the similarity in vibrational coupling (see the computation results below).

Isotopic labeled samples

Another strategy to suppress the energy transfer pathways is to decrease the Fermi resonance, or strong anharmonic coupling, present in the scaffold via isotopic labeling.[62] With this in mind, two more compounds containing triple-15N isotopic labeling of the N_3 group, ABS* and AMBS*, were synthesized and measured. In these labeled compounds, the N_3 vibrational frequency is shifted, thereby reducing the overlap of the nearly resonant dark ring modes. This isotopic labeling resulted in a red shift of the fundamental frequency by 55 and 67 cm^{-1} for ABS* (2037 cm^{-1}) and AMBS* (2031 cm^{-1}), respectively. The Fermi resonance transitions were also observed centered at 2070 and 2055 cm^{-1} for ABS* and AMBS*, respectively (see Fig. 4). It should be noted that a significant drop in intensity is also observed when compared to the unlabeled compounds mentioned in Fig. 3. The lack of energetic overlap between the combination bands of the ring modes and the fundamental N_3 stretch causes the coupling constant to decrease by a few wavenumbers, ~2–3 cm^{-1}. Akin to the previous compounds, the vibrational frequency of SeCN transitions remained unchanged at 2154 cm^{-1} for both ABS* and AMBS*.

For ABS*, a FWHM of 13.8 cm^{-1} was observed for the N_3 transition, showing a decrease of ~6 cm^{-1} when compared to the unlabeled ABS. On the other hand, the azide-transition of AMBS* has a FWHM of 26 cm^{-1}, which is more comparable to the bandwidth of the unlabeled AMBS compound. The Fermi resonance bandwidth significantly increased in both cases. The FWHM of the Fermi resonances increased by 12 cm^{-1} in ABS* and 21 cm^{-1} in AMBS* when compared to the unlabeled samples. The increased width is somewhat expected due to the lower intensity of the transitions and the reduced coupling. The IR intensity ratios between Fermi and N_3 were found to be 0.26:1 and 0.18:1 in ABS* and AMBS*, respectively. This follows our expectations that the intensities ratio between the N_3 and Fermi transitions decreases as a function of the isotopic labeling and reduction of the anharmonic coupling. It should be noted that an additional broadened vibrational transition is detected at 2107 cm^{-1}. This transition is likely due to additional Fermi resonance with different combination modes.[68] As expected, the FWHM of the SeCN transition remains unaffected by isotopic labeling.

2D IR measurements of ABS* showed a single strong transition along the diagonal observed at $\omega_t = \omega_\tau = 2040$ cm^{-1}, identified
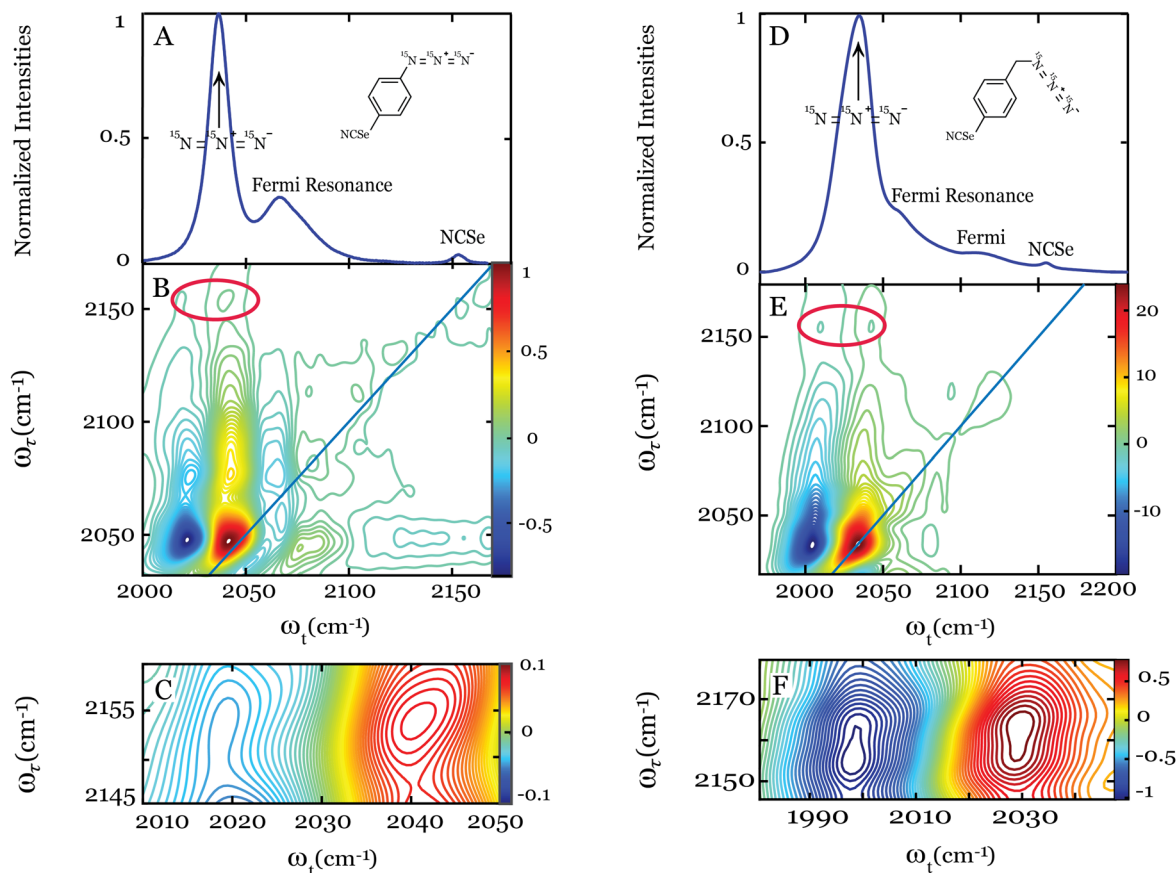

FIG. 4. FTIR spectra of (a) ABS* and (d) AMBS* in THF and absorptive 2D IR spectra of (b) ABS* and (e) AMBS* in THF at T = 200 fs. Figures (c) and (f) show the expanded cross-peak region of Figures (b) and (e), respectively.
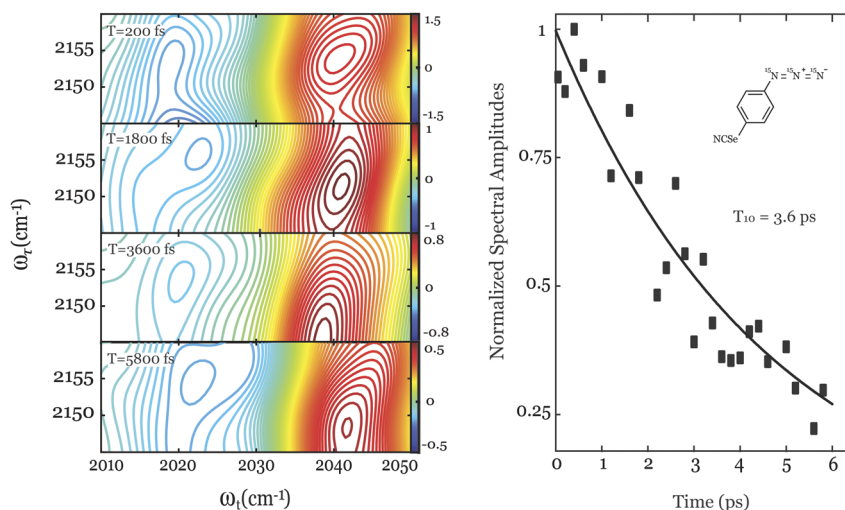
FIG. 5. (Left) Off-diagonal cross-peak region and (right) decay of cross-peak intensity as a function of waiting time of ABS*.

as the N_3 transition. The anharmonicity of this transition for ABS* is ~19.2 cm^{-1}. ABS* showed a much weaker Fermi resonance at $\omega_t = \omega_\tau = 2066$ cm^{-1} compared to ABS. Although the shifted N_3 transition decoupled the original dark ring modes, the shifted N_3 frequency became resonant with different combination modes of the ring, as computed in the DFT anharmonic frequency calculations. The density of states of the ring modes is very rich in this region of the spectrum. As a result of this anharmonic coupling, two sets of strong cross-peaks were observed on either side of the diagonal at $\omega_t = 2040$ cm^{-1}, $\omega_\tau = 2080$ cm^{-1}, as well as $\omega_t = 2082$ cm^{-1}, $\omega_\tau = 2040$ cm^{-1}. The anharmonic coupling strength of ~10.6 cm^{-1} (Table S1) again decreased slightly due to less overlap with these new combination bands of the ring. The vibrational lifetime was also measured for the N_3 transition to be ~1.56 ± 0.17 ps (Fig. S4). This population decay is ~5–6 times longer than the ABS scaffold most likely due to reduced anharmonic coupling via isotopic labeling of the N_3 group. A table of the population relaxations and cross-peak decays is included in the supplementary material (Table S2).

Furthermore, a larger dipolar coupling, ~33 cm^{-1}, was observed between the SeCN and the labeled N_3 group, likely due to more isolation of the vibrational oscillations involved. These cross-peaks are observed at $\{\omega_t, \omega_\tau\} = \{2041, 2154\}$ cm^{-1} in ABS*, highlighted by the red ovals in Fig. 4(b). Figure 5 shows the intensity decay of cross-peaks as a function of waiting time, T. The decay of these cross-peaks, indicative of anharmonically coupled modes, yields further evidence that the energy transfer pathway has been blocked. The time constant observed for the cross-peak decay is 3.6 ± 0.9 ps, limited by the vibrational lifetime of the N_3 transition of 1.56 ± 0.17 ps. A summary of the population relaxations and cross-peak decays is included in the supplementary material (Table S2).

Similarly, the N_3 transition for AMBS* was shifted to $\omega_t = \omega_\tau = 2031$ cm^{-1} as a result of isotopic labeling of the N_3 nitrogens, with a diagonal anharmonicity of 29.7 cm^{-1}. As before, the shift

in N_3 frequency did not completely remove the Fermi resonances; instead, different anharmonically coupled combination bands were observed at $\omega_t = \omega_\tau = 2107$ cm^{-1}. A coupling strength of ~10.4 cm^{-1} was determined from the corresponding cross-peaks at $\{\omega_t, \omega_\tau\} = \{2031, 2107\}$ cm^{-1}. The value was reduced for the unlabeled samples because of the decrease in resonance with the N_3 fundamental stretching transition. Another cross-peak was observed at $\{\omega_t, \omega_\tau\} = \{2031, 2154\}$ cm^{-1}, representing the coupling between the N_3 and the SeCN transitions. The measured coupling strength of ~38 cm^{-1} showed a twofold increase compared to the unlabeled AMBS.

The isotopic labeling was able to reduce the degree of anharmonic coupling between the N_3 and the dark ring modes. This reduction of the anharmonic coupling was sufficient to observe a significant increase in the vibrational coupling between the N_3 and SeCN transitions. However, due to the resonance with other combination bands of ring modes, the N_3 transition remained delocalized. Overall, based on the reduced anharmonic coupling caused by the shifted N_3 transitions, the decrease in intensity ratios of the N_3 to Fermi transition, and the gradual increase in vibrational lifetimes of the N_3 transition, a systematic trend was observed, showing increases in the dipolar coupling of the two fundamental transitions.

Coupling analysis and calculations

A scan of the dihedral angle between the benzene ring and the N_3 group was performed through a full rotation about the C–N bond (shown in Fig. 6) for both ABS and AMBS. At each angle, the geometry was allowed to relax to a minimum while the dihedral angle remained fixed. Since DFT methods do not consider isotopic effects on the total energy, the minimized structures of ABS* and AMBS* were the same as those for ABS and AMBS. The energy dependence about the dihedral angle resulted in two energetic minima along the potential energy surface (PES) for ABS, located at 180° and 360°, as expected based on the conjugation of the p-orbital on the internal
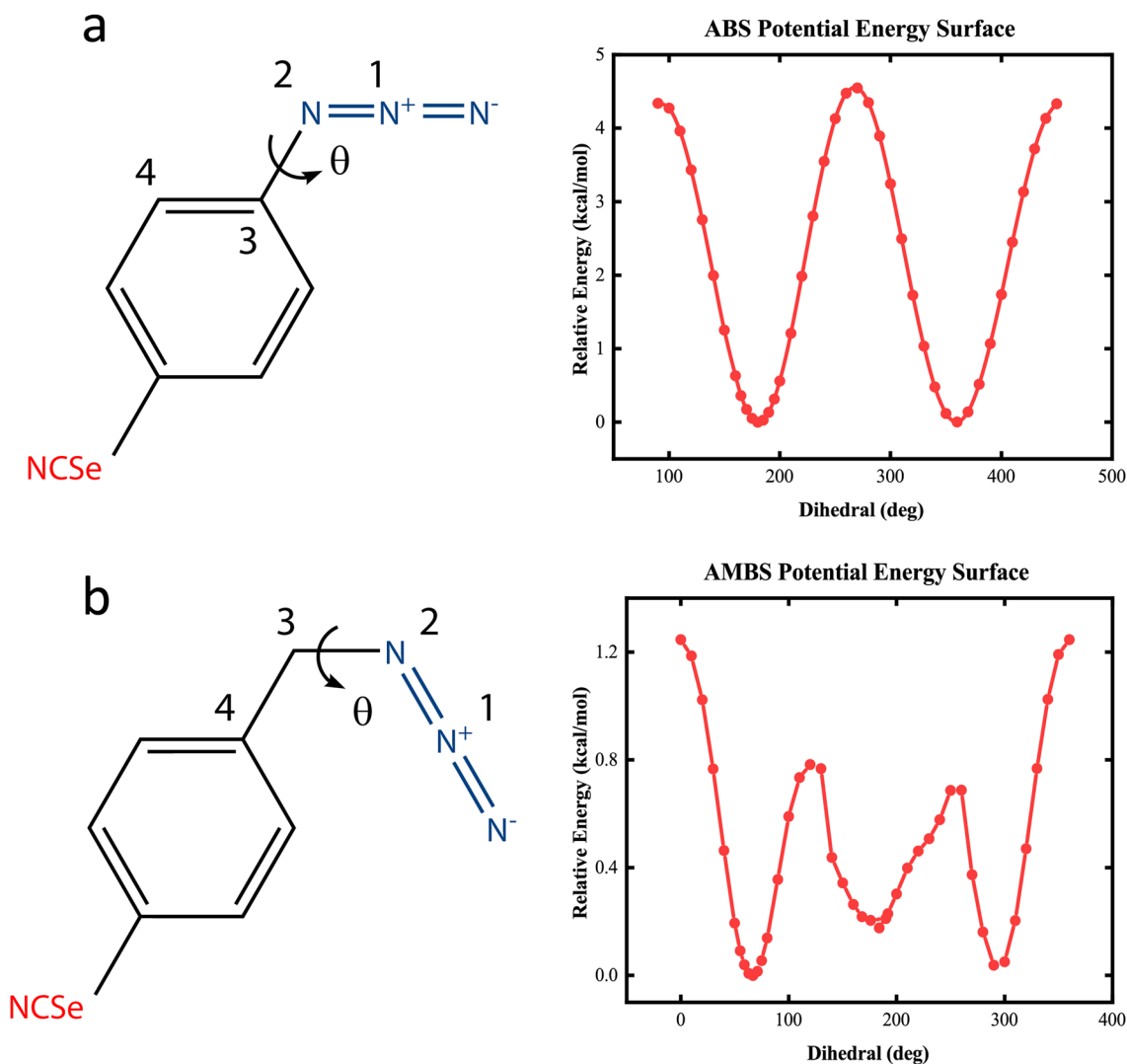
FIG. 6. (a) ABS and (b) AMBS molecules with the labeled atoms that represent the dihedral angle of interest and the calculated relative energies at different dihedral angles for (c) ABS and (d) AMBS.

N atom and the benzene ring. On the other hand, three local minima along the PES, located at $66°$, $178°$, and $290°$, were observed for AMBS (Fig. 6).

Note that all three minima of the PES for AMBS exist within the thermal equilibrium, defined to be below 0.59 kcal/mol at 298 K. The dipole moments, distances, orientation, and couplings were then calculated at each dihedral angle within the thermal distribution for ABS, AMBS, ABS*, and AMBS*. Since the PES for ABS was symmetric, only a sampling of the region between $160°$ and $200°$ is reported. The same region was used for ABS*. The average values found in the regions from $55°$ to $75°$ (region 1) and from $160°$ to $200°$ (region 2) are reported for AMBS and AMBS* and their corresponding thermal distributions.

The average dipole moment of the N_3 and SeCN transitions of ABS was found to be 0.547 ± 0.004 and 0.114 ± 0.002 D, respectively. The calculated average distance between dipoles for ABS was 6.12 ± 0.001 Å with an angle between dipoles of $101.2° \pm 10.5°$. The corresponding values found in AMBS for minima 1 were 0.429 ± 0.009 D and $0.118 \pm 0.8 \times 10^{-6}$ D for N_3 and SeCN transitions, respectively. The values in minima 2 for AMBS were found to be 0.481 ± 0.008 D and 0.118 ± 0.001 D for N_3 and SeCN, respectively. The average distances between dipoles for AMBS were 6.93 ± 0.005 and 6.94 ± 0.01 Å with the corresponding angles between dipoles found to be $36.0° \pm 0.8°$ and $68.8° \pm 7.4°$ in regions 1 and 2, respectively. Similar to ABS, the average dipole moments for ABS* were found to be 0.538 D and 0.117 D for the N_3 and SeCN

transitions, respectively, with an angle between dipoles of 105.6°. The dipole moments for AMBS* in minima 1 were found to be 0.408 D and 0.117 D for the N_3 and SeCN transitions, respectively. The values in minima 2 for AMBS* were found to be 0.460 D and 0.117 D for the N_3 and SeCN transitions, respectively. The average angle between dipoles was found to be 35.2° ± 1.1° and 67.8° ± 1.4° in regions 1 and 2, respectively. Overall, the dipole strengths and the distances between the dipoles do not vary much between the different samples. However, the orientation and angle between the dipoles are significantly different between the samples, leading to differences in their vibrational coupling.

The transition dipole coupling (TDC) theory was utilized to predict the interactions between the N_3 and SeCN transitions based on the calculated geometries and dipole moments. The average TDC coupling magnitude for ABS and ABS* was found to be ~1.55 cm^{-1}. The average TDC coupling value in AMBS and AMBS* was 0.4 cm^{-1} over both regions 1 and 2. Interestingly, the correct trend toward the lower coupling strength is observed for ABS compared to AMBS. However, the TDC model severely underestimated the measured experimental couplings between the two transitions. It is not unexpected since the TDC model is known to fail when the oscillation amplitude is comparable to the distance between the dipoles.[18,61,70] To accurately capture the coupling between the vibrational reporters, a more sophisticated model must be utilized.

Thus, the finite difference method (FDM) was employed to quantify the coupling from DFT calculations. This analytic coupling scheme is performed by estimating the second derivative of the PES with respect to the displacements in local modes of vibration,

$$\beta_{12} = \frac{\partial^2 V}{\partial Q_1 \partial Q_2}.$$

The central difference scheme was employed, and single-point energy calculations were performed after displacing the atoms in the molecules by 0.03 times the oscillation amplitude. The resulting coupling values were then averaged over small regions of the dihedral angle within the thermal equilibrium. The average FDM coupling strengths were also calculated in the same regions. The average value of the coupling was found to be 18.3 cm^{-1} in ABS and 9.8 cm^{-1} over both regions 1 and 2 of AMBS. As with TDC, the decrease in the vibrational coupling is accurately reproduced between ABS (~21 cm^{-1}) and AMBS (~19.6 cm^{-1}). The absolute magnitude of the coupling is accurate to ~87% for ABS and only ~50% for AMBS. The inaccuracies in the reproducibility likely stem from the multi-mode coupling that is present experimentally, i.e., the combination of Fermi coupling and dipolar coupling. For example, the delocalization of the N_3 transition (shown below) can play an important role. The coupling matrix would be more complex, generating different values than a traditional bilinear coupling model. The coupling strengths were not calculated for ABS* and AMBS* because the required DFT total energies do not consider isotopic effects.
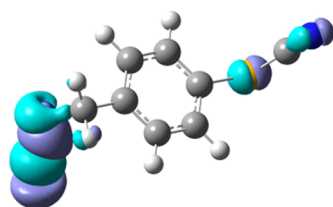
(a) ABS + 0.03 Å − N_3
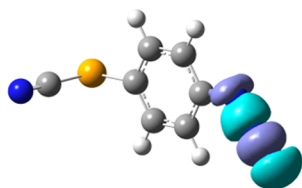
(b) ABS + 0.03 Å− SeCN
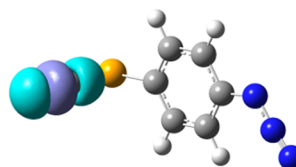
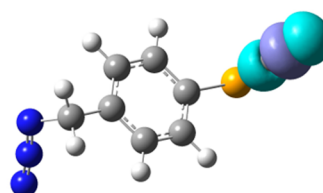(c) AMBS + 0.03 Å − N_3

(d) AMBS + 0.03 Å − SeCN

FIG. 7. Calculated transition densities of the N_3 and SeCN transitions of ABS (a) and (b) and AMBS (c) and (d) after perturbating the minimized structures +0.03 Å along the normal mode coordinates.

Each fundamental oscillation was investigated to determine how isolated the vibrational transition was from the rest of the molecule. Transition densities were calculated as the difference in electron density from equilibrium after a displacement of +0.03 Å. This perturbation was used to investigate the dependence of the transition density on the displacement from equilibrium. The resulting density plots are shown with an iso value of 0.003 esu/bohr in Fig. 7 for ABS and AMBS. From these plots, it is apparent that the SeCN transition is well localized to the CN atoms in both ABS and AMBS. However, the N_3 transition is somewhat delocalized in both ABS and AMBS, given that the transition density extends between the three nitrogen atoms of the azido group. The delocalization of the N_3 mode in both compounds indicates that the energy transfer pathway is still active between the N_3 transition and the benzene ring.

CONCLUSIONS

Several structural variations of the molecular scaffold were employed attempting to interrupt the thermal energy transfer pathways between the CN and N_3 moieties found in a prior study.[1] To assess these thermal energy pathways, an evolution of 2D IR cross-peaks was utilized to measure the changes in the energy flow across the molecule. The energy transfer pathway between the N_3 transition and the benzene ring remained intact despite isotopic labeling. The shifting of the vibrational frequencies via isotopic labeling could not remove the overlap with the ring modes due to the large density of states. However, taking advantage of the heavy atom effect provided by a selenium atom, the cyano-vibrational transition was isolated from the ring modes. By eliminating the anharmonic coupling to the ring, the energy transfer pathway through the entire molecule (N_3 to SeCN) was thus hindered and dipole–dipole coupling was facilitated. Thus, the vibrational coupling of a N_3/SeCN probe pair was observed for the first time. In addition, a method a developed to measure distances with these vibrational reporters in other larger scaffolds where energy transfer can be problematic and prevent such determination.

The N_3/SeCN coupling strength was directly related to the molecular structure, i.e., the angle between the dipoles and the distance between transitions. However, TDC did not accurately reproduce the magnitude of the experimentally observed coupling due to the similarity of the transition length compared to the distance between probes. The FDM was then utilized to compute the theoretical coupling values between the N_3 and SeCN vibrational reporters from single-point energy DFT calculations. The coupling strengths obtained from this method were in reasonable agreement with those obtained experimentally for ABS and AMBS. The coupling strengths of ABS* and AMBS* were not calculated because DFT total energies do not consider isotopic effects. Thus, the potential for rectification of this molecular circuitry was accomplished through the inhibition of energy flow using heavy atoms. This study was, thus, a proof of the principle that heavy atoms can sufficiently isolate specific vibrational modes, leading to the suppression of some transfer pathways (IVR) in favor of others (vibrational coupling).

SUPPLEMENTARY MATERIAL

The supplementary material contains details of the synthesis, determination of coupling strengths, decays of cross-peaks, vibrational lifetime decays, and polarization-controlled pump probe.

AUTHOR DECLARATIONS

Conflict of Interest

The authors have no conflicts to disclose.

Author Contributions

M.H. and C.J.M. contributed equally to the paper.

Majid Hassani: Data curation (equal); Formal analysis (equal); Investigation (equal); Validation (equal); Visualization (equal); Writing – original draft (supporting). **Christopher J. Mallon**: Data curation (equal); Formal analysis (equal); Investigation (equal); Validation (equal); Writing – review & editing (equal). **Judith N. Monzy**: Data curation (supporting); Investigation (supporting); Validation (supporting). **Andrew J. Schmitz**: Data curation (supporting); Methodology (supporting); Visualization (supporting). **Scott H. Brewer**: Funding acquisition (supporting); Writing – review & editing (supporting). **Edward E. Fenlon**: Conceptualization (equal); Funding acquisition (equal); Investigation (equal); Supervision (equal); Validation (equal); Writing – review & editing (equal). **Matthew J. Tucker**: Conceptualization (equal); Formal analysis (equal); Funding acquisition (equal); Investigation (equal); Methodology (equal); Project administration (equal); Resources (equal); Software (equal); Supervision (equal); Validation (equal); Visualization (equal); Writing – original draft (equal); Writing – review & editing (equal).

DATA AVAILABILITY

The data that support the findings of this study are available from the corresponding author upon reasonable request.

REFERENCES

[1] A. J. Schmitz et al., J. Phys. Chem. A **123**, 10571 (2019).
[2] P. Hamm et al., Proc. Natl. Acad. Sci. U. S. A. **96**, 2036 (1999).
[3] F. Chalyavi et al., Angew. Chem., Int. Ed. **57**, 7528 (2018).
[4] A. J. Schmitz et al., J. Phys. Chem. B **120**, 9387 (2016).
[5] H. T. Kratochvil et al., Science **353**, 1040 (2016).

[6] I. V. Rubtsov, Acc. Chem. Res. **42**, 1385 (2009).

[7] F. Chalyavi, O. Adeyiga, J. M. Weiner, J. N. Monzy, A. J. Schmitz, J. K. Nguyen, E. E. Fenlon, S. H. Brewer, S. O. Odoh, and M. J. Tucker, J. Chem. Phys. **152**, 074201 (2020).

[8] F. Chalyavi, A. J. Schmitz, and M. J. Tucker, J. Phys. Chem. Lett. **11**, 832 (2020).

[9] M. T. Zanni, Proc. Natl. Acad. Sci. U. S. A. **113**, 4890 (2016).

[10] N. H. C. Lewis et al., J. Phys. Chem. C **124**, 3470 (2020).

[11] J. S. Ostrander et al., J. Phys. Chem. B **121**, 1352 (2017).

[12] R. Yuan and M. D. Fayer, J. Phys. Chem. B **123**, 7628 (2019).

[13] S. Bagchi et al., J. Phys. Chem. B **113**, 8412 (2009).

[14] J. Zheng et al., Science **309**, 1338 (2005).

[15] F. Chalyavi, D. G. Hogle, and M. J. Tucker, J. Phys. Chem. B **121**, 6380 (2017).

[16] M. C. Asplund, M. T. Zanni, and R. M. Hochstrasser, Proc. Natl. Acad. Sci. U. S. A. **97**, 8219 (2000).

[17] L. P. DeFlores et al., J. Phys. Chem. B **110**, 18973 (2006).

[18] A. T. Krummel and M. T. Zanni, J. Phys. Chem. B **110**, 13991 (2006).

[19] A. M. Woys et al., J. Am. Chem. Soc. **134**, 19118 (2012).

[20] P. Hamm and M. Zanni, *Concepts and Methods of 2D Infrared Spectroscopy* (Cambridge University Press, 2012).

[21] A. Remorino and R. M. Hochstrasser, Acc. Chem. Res. **45**, 1896 (2012).

[22] A. Ghosh, M. J. Tucker, and R. M. Hochstrasser, J. Phys. Chem. A **115**, 9731 (2011).

[23] N. I. Rubtsova and I. V. Rubtsov, Annu. Rev. Phys. Chem. **66**, 717 (2015).

[24] H. Bian et al., J. Chem. Phys. **133**, 034505 (2010).

[25] X. He et al., J. Phys. Chem. B **121**, 9411 (2017).

[26] D. V. Kurochkin, S. R. G. Naraharisetty, and I. V. Rubtsov, Proc. Natl. Acad. Sci. U. S. A. **104**, 14209 (2007).

[27] D. M. Leitner, Annu. Rev. Phys. Chem. **59**, 233 (2008).

[28] D. M. Leitner and H. D. Pandey, Ann. Phys. **527**, 601 (2015).

[29] H. D. Pandey and D. M. Leitner, Chem. Phys. **482**, 81 (2017).

[30] D. M. Leitner and H. D. Pandey, J. Chem. Phys. **143**, 144301 (2015).

[31] H. Fujisaki and G. Stock, J. Chem. Phys. **129**, 134110 (2008).

[32] P. H. Nguyen, S.-M. Park, and G. Stock, J. Chem. Phys. **132**, 025102 (2010).

[33] B. C. Pein and D. D. Dlott, J. Phys. Chem. A **118**, 965 (2014).

[34] B. C. Pein, Y. Sun, and D. D. Dlott, J. Phys. Chem. A **117**, 6066 (2013).

[35] X. Dong et al., J. Phys. Chem. B **122**, 1296 (2018).

[36] F. Yang, J. Zhao, and J. Wang, J. Phys. Chem. B **120**, 1304 (2016).

[37] I. V. Rubtsov and R. M. Hochstrasser, J. Phys. Chem. B **106**, 9165 (2002).

[38] J. C. Owrutsky, D. Raftery, and R. M. Hochstrasser, Annu. Rev. Phys. Chem. **45**, 519 (1994).

[39] H. Bian, W. Zhao, and J. Zheng, J. Chem. Phys. **131**, 124501 (2009).

[40] H. T. Bian et al., J. Chem. Phys. **132** (2010).

[41] S. Rafiq et al., Chem **5**, 402 (2019).

[42] D. M. Leitner, Adv. Phys. **64**, 445 (2015).

[43] H. Bian et al., Proc. Natl. Acad. Sci. U. S. A. **108**, 4737 (2011).

[44] Z. Lin et al., Phys. Chem. Chem. Phys. **14**, 10445 (2012).

[45] V. M. Kasyanenko et al., J. Chem. Phys. **131**, 154508 (2009).

[46] H. Chen et al., J. Phys. Chem. B **119**, 4333 (2015).

[47] J. Li et al., J. Phys. Chem. B **117**, 4274 (2013).

[48] E. H. G. Backus et al., J. Phys. Chem. B **112**, 15487 (2008).

[49] H. M. Müller-Werkmeister and J. Bredenbeck, Phys. Chem. Chem. Phys. **16**, 3261 (2014).

[50] H. M. Müller-Werkmeister et al., Angew. Chem., Int. Ed. Engl. **52**, 6214 (2013).

[51] S. Kaziannis et al., Phys. Chem. Chem. Phys. **13**, 10295 (2011).

[52] M. Delor et al., J. Phys. Chem. B **118**, 11781 (2014).

[53] V. M. Kasyanenko et al., J. Phys. Chem. B **115**, 11063 (2011).

[54] S. R. G. Naraharisetty, V. M. Kasyanenko, and I. V. Rubtsov, J. Chem. Phys. **128**, 104502 (2008).

[55] N. I. Rubtsova et al., J. Phys. Chem. B **118**, 8381 (2014).

[56] A. V. Kachanov et al., Tetrahedron Lett. **45**, 4461 (2004).

[57] Y. S. Kim and R. M. Hochstrasser, J. Phys. Chem. B **109**, 6884 (2005).

[58] Y. S. Kim, J. Wang, and R. M. Hochstrasser, J. Phys. Chem. B **109**, 7511 (2005).

[59] C. Fang and R. M. Hochstrasser, J. Phys. Chem. B **109**, 18652 (2005).

[60] M. J. Frisch et al., Gaussian 16 Rev. C.01 (Wallingford, CT, 2016).

[61] A. Moran and S. Mukamel, Proc. Natl. Acad. Sci. U. S. A. **101**, 506 (2004).

[62] J. S. Lipkin et al., J. Phys. Chem. Lett. **2**, 1672 (2011).

[63] J. Zhang et al., J. Phys. Chem. B **122**, 8122 (2018).

[64] M. Maj et al., Phys. Chem. Chem. Phys. **17**, 11770 (2015).

[65] X. S. Gai et al., Phys. Chem. Chem. Phys. **13**, 5926 (2011).

[66] F. Chalyavi et al., Phys. Chem. Chem. Phys. **22**, 18007 (2020).

[67] D. E. Levin et al., RSC Adv. **6**, 36231 (2016).

[68] C. Varner et al., Chem. Phys. **512**, 20 (2018).

[69] S. M. Fica-Contreras et al., J. Phys. Chem. B **125**, 8907 (2021).

[70] A. T. Krummel and M. T. Zanni, J. Phys. Chem. B **112**, 1336 (2008).